




Discovery of WASP-174b: Doppler tomography of a near-grazing transit

L. Y. Temple,¹ C. Hellier,¹ Y. Almleaky,^{2,3} D. R. Anderson,¹ F. Bouchy,⁴
 D.J.A. Brown ,^{5,6} A. Burdanov,⁷ Collier Cameron ,⁸ L. Delrez,⁹ M. Gillon,⁷
 R. Hall ,⁹ E. Jehin,⁷ M. Lendl,^{4,10} P.F.L. Maxted,¹ L. D. Nielsen,⁴ F. Pepe,⁴
 D. Pollacco,^{5,6} D. Queloz,⁹ D. Ségransan,⁴ B. Smalley,¹ S. Sohy,⁷ S. Thompson,⁹
 A.H.M.J. Triaud,¹¹ O.D. Turner,^{1,4} S. Udry⁴ and R.G. West⁵

¹*Astrophysics Group, Keele University, Staffordshire ST5 5BG, UK*

²*Space and Astronomy Department, Faculty of Science, King Abdulaziz University, 21589 Jeddah, Saudi Arabia*

³*King Abdullah Centre for Crescent Observations and Astronomy (KACCOA), Makkah Clock, Saudi Arabia*

⁴*Observatoire astronomique de l'Université de Genève 51 ch. des Maillettes, CH-1290 Sauverny, Switzerland*

⁵*Department of Physics, University of Warwick, Gibbet Hill Road, Coventry CV4 7AL, UK*

⁶*Centre for Exoplanets and Habitability, University of Warwick, Gibbet Hill Road, Coventry CV4 7AL, UK*

⁷*Space sciences, Technologies and Astrophysics Research (STAR) Institute, Université de Liège, Allée du 6 Août 17, B-4000 Liège, Belgium*

⁸*SUPA, School of Physics and Astronomy, University of St. Andrews, North Haugh, Fife KY16 9SS, UK*

⁹*Cavendish Laboratory, J J Thomson Avenue, Cambridge CB3 0HE, UK*

¹⁰*Space Research Institute, Austrian Academy of Sciences, Schmiedlstraße 6, A-8042 Graz, Austria*

¹¹*School of Physics & Astronomy, University of Birmingham, Edgbaston, Birmingham B15 2TT, UK*

Accepted 2018 August 8. Received 2018 August 8; in original form 2018 February 2

ABSTRACT

We report the discovery and tomographic detection of WASP-174b, a planet with a near-grazing transit on a 4.23-d orbit around a $V = 11.9$, F6V star with $[\text{Fe}/\text{H}] = 0.09 \pm 0.09$. The planet is in a moderately misaligned orbit with a sky-projected spin–orbit angle of $\lambda = 31^\circ \pm 1^\circ$. This is in agreement with the known tendency for orbits around hotter stars to be misaligned. Owing to the grazing transit, the planet’s radius is uncertain with a possible range of 0.8–1.8 R_{Jup} . The planet’s mass has an upper limit of 1.3 M_{Jup} . WASP-174 is the faintest hot-Jupiter system so far confirmed by tomographic means.

Key words: techniques: photometric – techniques: spectroscopic – planetary systems – stars: rotation.

1 INTRODUCTION

Hot-Jupiter exoplanets orbiting stars of A–mid-F spectral types, which lie beyond the Kraft break at $T_{\text{eff}} > 6250$ K (Kraft 1967), are likely to have different properties from those orbiting cooler stars. First, planets with hot stars will be more highly irradiated, producing hotter and sometimes ‘ultra-hot’ Jupiters (with $T_{\text{eq}} \gtrsim 2200$ K). The high irradiation is also thought to be related to the inflated radii seen in many hot Jupiters (e.g. Hartman et al. 2016). Secondly, hot Jupiters transiting hotter stars are more likely to be in misaligned orbits, a trait which was first noted by Winn et al. (2010) and has been discussed at length in recent literature (e.g. Valsecchi & Rasio 2014; Mazeh et al. 2015; Dai & Winn 2017; for a review, see Triaud 2017). And thirdly, where early-type stars are fast rotators, the rotation period can be shorter than the planet’s orbital period, giving a systematically different tidal interaction than in most hot-Jupiter systems (see e.g. Crouzet et al. 2017). It is important to understand these differences in order

to create a complete picture of how planetary systems form and evolve.

Another difference between hot Jupiters and ultra-hot Jupiters is the efficiency with which heat can be transported from the tidally locked dayside of the planet to its nightside. More highly irradiated planets are less efficient at recirculating heat within the atmosphere: ultra-hot Jupiters have dayside temperatures close to the local radiative equilibrium temperature (Heng & Showman 2015), indicative of inefficient transport of heat to the nightside.

The inflated radii of hot Jupiters make them ideal candidates for studying planetary atmospheres using transmission spectroscopy (e.g. Kreidberg et al. 2015; Wyttenbach et al. 2015; Gibson et al. 2017; Yan & Henning 2018) while the high surface temperatures make it possible to observe the thermal emission of these planets in the infrared (e.g. Gillon et al. 2010; Stevenson et al. 2014).

High irradiation, combined with absorption by molecules such as TiO and VO, is expected to produce a thermal inversion in the upper atmosphere (Fortney et al. 2008), and this has been found in some ultra-hot Jupiters (e.g. WASP-121b; Evans et al. 2017) but not in others (e.g. Kepler-13Ab; Beatty et al. 2017). In WASP-103b, Kreidberg et al. (2018a) find an inversion on the irradiated

* E-mail: l.y.temple@keele.ac.uk

dayside of the planet but not on the cooler nightside. Water features can be prominent in the spectra of cooler hot Jupiters (e.g. WASP-107b; Kreidberg et al. 2018b), but may be absent on the dayside of hotter planets such as WASP-18b and WASP-103b, which instead show relatively featureless blackbody spectra. The difference can be attributed to the water molecules disassociating on the dayside of ultra-hot Jupiters, and to the presence of opacity owing to H⁻ ions (Arcangeli et al. 2018; Kreidberg et al. 2018a; Parmentier et al. 2018).

Hot, fast-rotating stars usually give poor radial-velocity measurements owing to their broad and weak spectral lines. This means that planets around such stars are often confirmed by Doppler tomography of the stellar line profiles through a transit. This method involves detecting the perturbation to stellar line profiles that occurs during transit due to the planet blocking a portion of the Doppler-shifted stellar light.

The first planet discovered in this way was WASP-33b (Collier Cameron et al. 2010b), while recently such discoveries include: XO-6b (Crouzet et al. 2017), KELT-17b (Zhou et al. 2016a), KELT-9b (Gaudi et al. 2017), KELT-19Ab (Siverd et al. 2018), KELT-20b/MASCARA-2b (Lund et al. 2017; Talens et al. 2018), KELT-21b (Johnson et al. 2018), HAT-P-57b (Hartman et al. 2015), HAT-P-67b (Zhou et al. 2017), Kepler-448b (Bourrier et al. 2015), WASP-167b/KELT-13b (Temple et al. 2017) and MASCARA-1b (Talens et al. 2017).

We report here the discovery of a hot Jupiter found as a candidate in the WASP-South transit survey (Hellier et al. 2011) and confirmed by Doppler tomography using the ESO 3.6-m/HARPS spectrograph (Pepe et al. 2002), together with follow-up photometry from the TRAPPIST-South and SPECULOOS-Europa telescopes (Jehin et al. 2011; Burdanov et al. 2017). The methods used here are similar to those used for WASP-167b/KELT-13b (Temple et al. 2017), but we provide key details of the analysis in Sections 3–5.

2 OBSERVATIONS

The discovery photometry for WASP-174b was obtained using WASP-South, an array of eight cameras based at the South African Astronomical Observatory (SAAO), from 2006 May–2012 June. We used 30-s exposures and typically 10-minute cadence with a 400–700 nm broad-band filter. WASP-South data are reduced as explained by Collier Cameron et al. (2006) while the candidate selection process is explained by Collier Cameron et al. (2007).

Following the detection of a planet-like transit signal with a ~ 4 -day period, we selected the object for our followup programme. While the dip is V-shaped, more typical of an eclipsing binary than a planet transit, such dips are also produced by planet transits with a high impact factor. Rejecting eclipsing-binary mimics usually takes only one or two spectra, and so we don't reject V-shaped candidates from WASP follow-up.

We thus obtained 16 radial-velocity measurements using the Euler/CORALIE spectrograph (Queloz et al. 2001). These were compatible with the transiting object being a planet, however, the broad spectral features meant that the error bars are large and thus could not produce a secure orbital variation and hence a mass. To confirm the planet, we therefore decided to also use Doppler tomography, and observed a series of 23 spectra with the HARPS spectrograph covering a transit on the night of 2016 March 13. Simultaneously with this, we observed the transit photometrically with TRAPPIST-South. Details of the observations are given in Table 1 while the measured radial velocities are given in Table 2.

Table 1. Details of all observations of WASP-174b used in this work, including the discovery photometry, the follow-up photometry and the spectroscopic observations.

Facility	Date	Notes
WASP-South	2006-05– 2012-06	35 883 points
TRAPPIST-South	2014-03-20	I+z'. 14s exp.
TRAPPIST-South	2016-03-13	I+z'. 8s exp.
TRAPPIST-South	2017-03-08	V. 15s exp.
SPECULOOS-Europa	2017-07-13	I+z'. 10s exp.
CORALIE	2014-03– 2017-08	16 out-of-transit spectra
HARPS	2016-03-13	23 spectra taken including a transit

Table 2. Radial velocities and bisector spans for WASP-174b.

BJD (TDB –2450000)	RV (km s ⁻¹)	σ_{RV} (km s ⁻¹)	BS (km s ⁻¹)	σ_{BS} (km s ⁻¹)
CORALIE RVs:				
6719.750940	4.87	0.05	–0.28	0.10
6770.634386	4.91	0.05	–0.15	0.10
6836.575290	4.84	0.09	0.11	0.18
7072.738390	4.71	0.06	0.17	0.12
7888.597863	4.79	0.09	–0.21	0.18
7890.515926	4.73	0.14	0.24	0.28
7894.502532	4.79	0.08	–0.10	0.16
7903.605663	4.66	0.13	–0.42	0.26
7905.689111	4.85	0.07	–0.30	0.14
7917.567974	4.85	0.07	–0.06	0.14
7924.505661	4.82	0.06	–0.35	0.12
7951.506527	4.73	0.17	–0.41	0.34
7954.495100	4.83	0.07	0.01	0.14
7959.517031	4.70	0.09	–0.03	0.18
7973.492569	4.82	0.12	0.17	0.24
7974.518841	4.65	0.09	–0.16	0.18
HARPS RVs:				
7461.571827	4.87	0.02	–0.09	0.04
7461.582499	4.89	0.02	–0.16	0.04
7461.593380	4.88	0.02	–0.09	0.04
7461.604248	4.85	0.02	–0.16	0.04
7461.615140	4.89	0.02	–0.15	0.04
7461.625708	4.86	0.02	–0.10	0.04
7461.636692	4.85	0.02	–0.12	0.04
7461.647260	4.89	0.02	–0.10	0.04
7461.657920	4.86	0.02	–0.03	0.04
7461.668696	4.88	0.02	–0.14	0.04
7461.679576	4.83	0.02	–0.09	0.04
7461.690352	4.78	0.02	0.12	0.04
7461.701024	4.77	0.01	0.07	0.02
7461.711800	4.79	0.01	–0.03	0.02
7461.722576	4.78	0.02	–0.13	0.04
7461.733457	4.81	0.01	–0.15	0.02
7461.743804	4.83	0.02	–0.10	0.04
7461.754893	4.84	0.02	–0.00	0.04
7461.765565	4.88	0.02	–0.10	0.04
7461.776549	4.85	0.02	–0.19	0.04
7461.787013	4.87	0.02	–0.15	0.04
7461.797985	4.87	0.02	–0.02	0.04
7461.808866	4.84	0.02	–0.19	0.04

We have also obtained photometry of three other transits with TRAPPIST-South and SPECULOOS-Europa (see Table 1). While TRAPPIST-South has been used extensively for the discovery and parametrization of WASP planets (Gillon et al. 2012), this is the first WASP paper to feature data from the newer SPECULOOS, so we describe it briefly.

The SPECULOOS-Europa telescope is one of four identical telescopes currently being installed at ESO Paranal Observatory. SPECULOOS is a ground-based transit survey that will search for Earth-sized planets transiting the nearest ultracool dwarfs (Burdanov et al. 2017). Each SPECULOOS telescope is a robotic Ritchey–Chretien (F/8) telescope of 1-m diameter. They are equipped with Andor Peltier-cooled deeply depleted $2K \times 2K$ CCD cameras, with 13.5 micron pixels. The field of view of each telescope is $12 \text{ arcmin} \times 12 \text{ arcmin}$ and the corresponding pixel scale is $0.35 \text{ arcmin pixel}^{-1}$.

Lastly, we report that we searched the WASP photometry looking for stellar rotational modulations in the range 0–1.5 cycles day^{-1} , using the methods of Maxted et al. (2011). We did not detect any modulations, or evidence of pulsations, with an upper limit of 0.8 mmag.

3 SPECTRAL ANALYSIS

We performed a spectral analysis on a median-stacked HARPS spectrum created from the 23 we obtained, in order to determine some stellar properties. We follow the method described by Doyle et al. (2013) to determine values for the stellar effective temperature T_{eff} , stellar surface gravity $\log g_*$, the stellar metallicity $[\text{Fe}/\text{H}]$, the stellar lithium abundance $\log A(\text{Li})$, and the projected stellar rotational velocity $v \sin i_*$. To constrain the latter, we obtain a macroturbulence value of $v_{\text{mac}} = 6.3 \text{ km s}^{-1}$ using the Doyle et al. (2014) calibration. T_{eff} was measured using the H α line while $\log g_*$ was measured from the Na D lines. We also determine the spectral type of the star to be F6V, by using the MKCLASS program (Gray & Corbally 2014). The values obtained for each of the fitted parameters are given in Table 3.

4 COMBINED ANALYSES

We performed a Markov Chain Monte Carlo (MCMC) fitting procedure which uses the stellar parameters obtained in the spectral analysis (Section 3) to constrain the fit. We used the latest version of the MCMC code described by Collier Cameron et al. (2007) and Pollacco et al. (2008), which is capable of fitting photometric, RV, and tomographic data simultaneously (Collier Cameron et al. 2010a).

The system parameters which are determined from the photometric data are the epoch of mid-transit T_c , the orbital period P , the planet-to-star area ratio $(R_p/R_*)^2$, the transit duration T_{14} , and the impact parameter b . Limb darkening was accounted for using the Claret (2000, 2004) four-parameter non-linear law: for each new value of T_{eff} a set of parameters is interpolated from the Claret tables. The proposed values of the stellar mass are calculated using the Enoch–Torres relation (Enoch et al. 2010; Torres, Andersen & Giménez 2010).

The RV fitting then provides values for the stellar reflex velocity semi-amplitude K_1 and the barycentric system velocity γ . We assume a circular orbit, since we do not have sufficient quality in the out-of-transit RVs to constrain the eccentricity. In any case, hot Jupiters often settle into circular orbits on time-scales that are shorter than their lifetimes through tidal circularization (Pont et al.

Table 3. All system parameters obtained for WASP-174b in this work.

1SWASP J130310.57–412305.3		
2MASS J13031055–4123053		
TIC ID:102192004		
RA = $13^{\text{h}}03^{\text{m}}10.57^{\text{s}}$, Dec = $-41^{\circ}23'05.3''$ (J2000)		
$V=11.9$ (NOMAD)		
IRFM $T_{\text{eff}}=6380 \pm 140 \text{ K}$		
IRFM $\theta=0.031 \pm 0.002 \text{ mas}$		
<i>Gaia</i> DR2 Proper Motions:		
(RA) 0.043 ± 0.071 (Dec) $-5.784 \pm 0.112 \text{ mas yr}^{-1}$		
<i>Gaia</i> DR2 Parallax: $2.41 \pm 0.06 \text{ mas}$		
Rotational Modulations: $<0.8 \text{ mmag}$ (95%)		
<i>Stellar parameters from spectral analysis:</i>		
Parameter	Value	
(Unit)		
Spectral type	F6V	
T_{eff} (K)	6400 ± 100	
$\log g_*$	4.15 ± 0.15	
$[\text{Fe}/\text{H}]$	0.09 ± 0.09	
$\log A(\text{Li})$	2.48 ± 0.10	
$v \sin i_*$ (km s^{-1})	16.5 ± 0.5	
v_{mac} (km s^{-1})	6.3	
<i>Parameters from photometric and RV analysis:</i>		
Parameter	DT Value	RM Value:
(Unit)	(adopted):	
P (d)	$4.233\,700 \pm 0.000\,003$	$4.233\,700 \pm 0.000\,003$
T_c (BJD _{TDB})	$2\,457\,465.933\,6 \pm 0.000\,42$	$2\,457\,465.933\,5 \pm 0.000\,4$
T_{14} (d)	0.085 ± 0.002	0.085 ± 0.002
R_p^2/R_*^2	$0.008\,6 \pm 0.000\,3$	$0.008\,8 \pm 0.000\,6$
b	0.94 ± 0.03	0.95 ± 0.04
i ($^\circ$)	84.2 ± 0.5	84.0 ± 0.7
a (au)	$0.055\,9 \pm 0.000\,9$	$0.055\,5 \pm 0.000\,9$
M_* (M_\odot)	1.30 ± 0.06	1.31 ± 0.07
R_* (R_\odot)	1.31 ± 0.08	1.3 ± 0.1
$\log g_*$ (cgs)	4.32 ± 0.04	4.31 ± 0.06
ρ_* (ρ_\odot)	0.6 ± 0.2	0.6 ± 0.1
T_{eff} (K)	$6\,400 \pm 100$	$6\,400 \pm 100$
$[\text{Fe}/\text{H}]$	0.09 ± 0.09	0.09 ± 0.09
M_p (M_{Jup})	< 1.3 (95%)	< 1.3 (95%)
K (km s^{-1})	< 0.14 (95%)	< 0.14 (95%)
R_p (R_{Jup})	1.3 ± 0.5	1.4 ± 0.5
T_{eq} (K)	$1\,490 \pm 50$	$1\,500 \pm 60$
<i>Parameters from RM and DT analyses:</i>		
γ (km s^{-1})	4.864 ± 0.005	4.860 ± 0.004
λ ($^\circ$)	31 ± 1	34 ± 5
<i>Parameters from BAGEMASS:</i>		
Parameter	Value	
(Unit)		
Age (Gyr)	1.65 ± 0.85	
M_* (M_\odot)	1.28 ± 0.07	
$[\text{Fe}/\text{H}]_{\text{init}}$	0.12 ± 0.08	

2011), so usually their orbits are circular. If there are accurate RVs taken through transit, it is also possible to measure the projected spin-orbit misalignment angle λ by fitting the Rossiter–McLaughlin (RM) effect.

The 23 HARPS spectra were cross-correlated using the standard HARPS Data Reduction Software over a window of $\pm 350 \text{ km s}^{-1}$ (as described in Baranne et al. 1996; Pepe et al. 2002). The cross-correlation functions (CCFs) were created using a mask matching a G2 spectral type, containing zeroes at the positions of absorption lines and ones in the continuum. The tomographic data are then comprised of the time series of CCFs taken through tran-

sit. The CORALIE spectra were also correlated using the same methodology.

We used the MCMC code in two modes. The first mode fits the CCFs to obtain RV values, and then uses the calibrations of Hirano et al. (2011) to model the RM effect and thus measure λ . The second mode fits the in-transit CCFs directly, modelling the perturbations of the CCFs due to the path of the planet across the stellar disc (e.g. Brown et al. 2017; Temple et al. 2017). The parameters determined in this part of the analysis are $v \sin i_*$, λ , the stellar line-profile Full-Width at Half-Maximum (FWHM), the FWHM of the line perturbation due to the planet v_{FWHM} and the system γ -velocity. The MCMC code assumes a Gaussian shape for the line perturbation caused by the planet. We obtain initial values for the stellar line FWHM and the γ -velocity by fitting a Gaussian profile to the CCFs and apply the spectral $v \sin i_*$ and T_{eff} as priors. Neither λ nor v_{FWHM} had a prior applied.

We give the solutions obtained using the two modes in Table 3. Both fits gave strongly consistent results. We adopt the solution of the fit including tomography, since it is a more direct method that uses more of the line-profile information.

4.1 A grazing transit

The photometry and the best-fitting model are shown in Fig. 1. We found that constraining the photometric fit was difficult since the transit is either grazing or near-grazing and does not show clear second and third contacts. This means that R_p/R_* and the impact parameter b are poorly constrained. We show the probability distributions of R_p , R_* , and b in Fig. 2.

We calculated the ‘grazing criterion’, namely $(R_p/R_* + b)$, which if > 1 implies a grazing transit (Smalley et al. 2011). We obtain $1.02^{+0.04}_{-0.02}$, which means that we cannot securely distinguish between grazing and near-grazing solutions.

We used the InfraRed Flux Method (IRFM; Blackwell & Shallis 1977) to obtain values for T_{eff} and the angular diameter θ of WASP-174 which are quoted in Table 3. We then used θ and the *Gaia* DR2 (*Gaia* Collaboration et al. 2016, 2018) parallax, which is also quoted in Table 3, to estimate the stellar radius. We took reddening into account by measuring the equivalent width of the interstellar Na D lines using the stacked HARPS spectrum from Section 3, finding a width of 80 mÅ which equates to an extinction value of $E(B - V) = 0.02$ (Munari & Zwitter 1997). We have also taken into account the systematic offset in the *Gaia* parallax value (of 0.082 mas), as measured by Stassun & Torres (2018). We obtain a stellar radius of $1.35 \pm 0.10 R_{\odot}$, which is consistent with our fitted radius of $1.31 \pm 0.08 R_{\odot}$.

4.2 The planet’s mass

The CORALIE and HARPS RVs are shown in Fig. 3. Due to the relatively large error bars in the out-of-transit RV measurements, we do not regard the fitted semi-amplitude (of $0.08 \pm 0.03 \text{ km s}^{-1}$) to be a measure of the planet’s mass. However, we were able to put a 95 per cent confidence upper limit on the mass of $1.3 M_{\text{Jup}}$, and the predicted curve for this value is also shown in Fig. 3.

4.3 The Doppler track

We display the tomographic data as a function of the planet’s orbital phase in Fig. 4. In creating this plot, we first remove the invariant stellar line profile by subtracting the average of the out-of-transit CCFs. We also display the simultaneous photometric observation

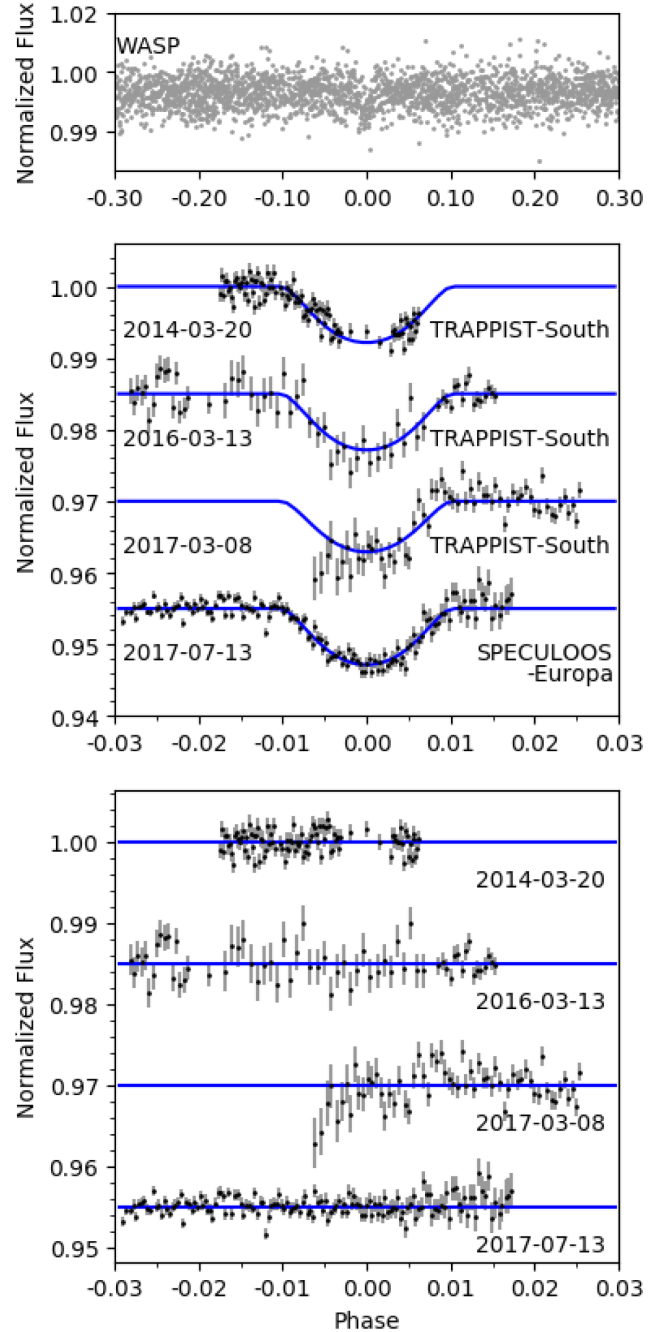


Figure 1. The WASP discovery photometry (top) and follow-up transit light curves (middle). The blue lines show the final model obtained in the MCMC fitting (see Section 4). The bottom panel then shows the residuals of the fit.

to the left of the tomogram, and the residuals from subtracting the planet model on the right.

We interpret the resulting tomogram as showing a faint, prograde-moving planet signal crossing only the red-shifted portion of the plot. This is in line with the transit being grazing, such that the planet crosses only a short chord on the face of the star (see Fig. 5).

The planet’s Doppler shadow appears very faint at the beginning and end of the transit (see Fig. 4). This is likely due to there being little of the planet on the face of the star near first and fourth contacts, owing to the near-grazing nature of the orbit.

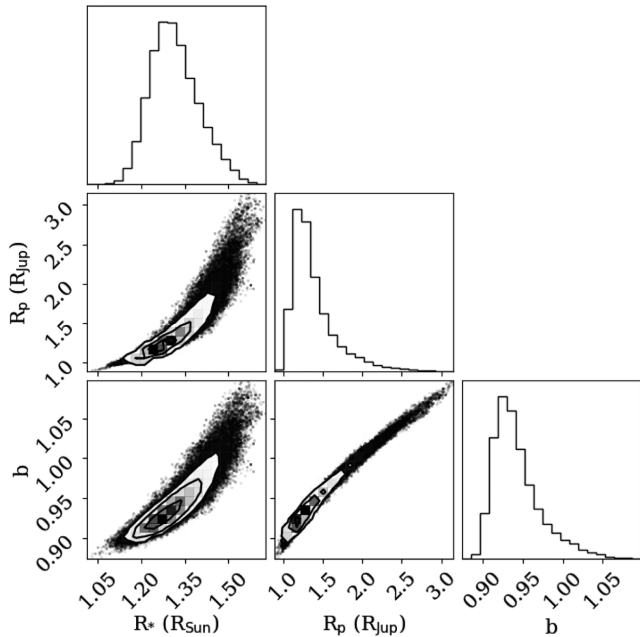


Figure 2. Probability distributions for the parameters R_p , R_* , and b , created from the results of the second-mode MCMC run.

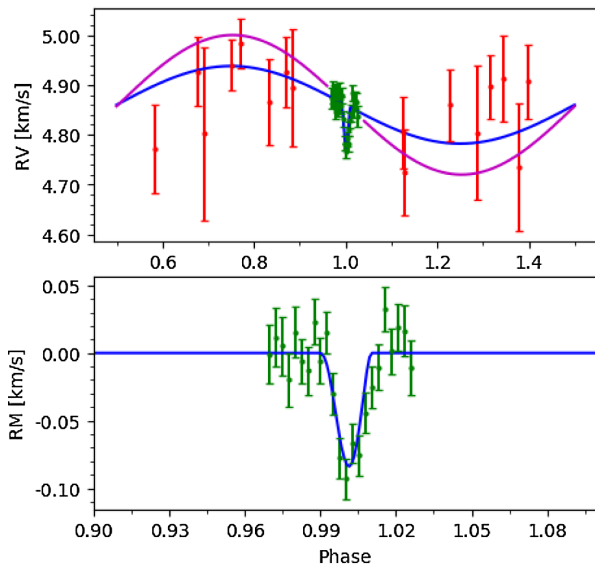


Figure 3. Top: The 16 CORALIE RVs (red points) obtained for WASP-174b. The magenta line shows the expected RV amplitude for a planet of $1.3 M_{\text{Jup}}$, our derived upper limit (95 per cent confidence). The blue line shows the best-fitting model including the RM fit. Bottom: The 23 through-transit HARPS RVs (green points). The blue line shows the best-fitting model with the Keplerian RV curve subtracted, leaving only the fit to the RM effect.

5 STELLAR AGE DETERMINATION

We estimated the age of WASP-174 using the open source software BAGEMASS.¹ BAGEMASS uses the Bayesian method of Maxted, Serenelli & Southworth (2015) to fit the age, mass, and initial metallicity of a star using the GARSTEC stellar evolution code (Weiss

& Schlattl 2008). We applied constraints on the stellar temperature and metallicity ($T_{\text{eff}} = 6400 \pm 100$ K and $[\text{Fe}/\text{H}] = 0.09 \pm 0.09$ as obtained in the spectral analysis) as well as the stellar density ($\rho_*/\rho_{\odot} = 0.6 \pm 0.2$ from the transit analysis). We adopt the solution obtained for a solar mixing length and He abundance, since enhancing the He abundance made no significant change to the fit while reducing the solar mixing length worsened the fit. We display the resulting isochrones and evolutionary tracks for this fit in Fig. 6 and the fitted values are given in Table 3.

We find WASP-174 to be consistent with a main-sequence star or one beginning to evolve off the main sequence. The Li abundance obtained in Section 3 is also consistent with the star being non-evolved, but for mid-F stars the Li abundance is not a good age indicator. For the measured value of $\log A(\text{Li}) = 2.48 \pm 0.10$, WASP-174 could be up to a few Gyr old (Sestito & Randich 2005). If we define the main-sequence lifetime of a star to be the time taken for all hydrogen in the core to be exhausted, we can use the best-fitting evolutionary track from BAGEMASS to estimate the age at which WASP-174 will leave the main sequence: 4.3 ± 0.6 Gyr.

6 DISCUSSION AND CONCLUSIONS

WASP-174b is revealed by Doppler tomography to be a planet making a grazing transit of its host star in a misaligned orbit with an alignment angle of $\lambda = 31^\circ \pm 1^\circ$.

WASP-174 is an F6 star with an effective temperature of $T_{\text{eff}} = 6400 \pm 100$ K and a measured $v \sin i_*$ of 16.5 ± 0.5 km s⁻¹. This rotation rate, together with a fitted radius of $1.31 \pm 0.08 R_{\odot}$, implies a stellar rotation period of $P_{\text{rot}} < 4.4$ d. Since the planet's orbital period is 4.23 d, this means that the stellar rotation period could be, but is not certain to be, shorter than the planet's orbit. Most hot-Jupiter systems have rotation periods that are longer than the orbit, but having $P_{\text{orb}} > P_{\text{rot}}$ has been found for other hot, more rapidly rotating host stars, including KELT-17b (Zhou et al. 2016a), WASP-167b/KELT-13b (Temple et al. 2017), and XO-6b (Crouzet et al. 2017). In systems with $P_{\text{orb}} < P_{\text{rot}}$ and with prograde orbits the tidal interaction is thought to produce decay of the planet's orbit, but this will be reversed in systems such as WASP-174, with a prograde orbit and with $P_{\text{orb}} > P_{\text{rot}}$ (see the discussions in Crouzet et al. 2017 and Temple et al. 2017). The difference in dynamical evolution of hot-star hot Jupiters makes them interesting targets and is one reason for finding more examples of such systems.

Another dynamical difference is that hot-Jupiter orbits are much more likely to be misaligned around hotter stars, which might be related to reduced tidal damping in hotter stars with smaller or absent convective envelopes (Winn et al. 2010). With a misaligned orbit WASP-174b is in line with this trend. Of the 12 other systems confirmed with tomographic methods, 8 are at least moderately misaligned. These are WASP-33b (Collier Cameron et al. 2010b), HAT-P-57b (Hartman et al. 2015), KELT-17b (Zhou et al. 2016a), KELT-9b (Gaudi et al. 2017), KELT-19Ab (Siverd et al. 2018), XO-6b (Crouzet et al. 2017), WASP-167b/KELT-13b (Temple et al. 2017), and MASCARA-1b (Talens et al. 2017).

High stellar irradiation produces hotter planetary atmospheres, and is thought to result in the inflated radii seen in many hot Jupiters (e.g. Hartman et al. 2016; Zhou et al. 2017; Siverd et al. 2018). With an equilibrium temperature of 1490 ± 50 K, we would thus expect WASP-174b to be moderately inflated.

The actual planetary radius is hard to measure owing to the grazing or near-grazing transit, which means that second and third contacts are not visible in the transit profile and the fitted radius is degenerate with the impact parameter (Fig. 2). Thus, we can do no

¹<http://sourceforge.net/projects/bagemass>

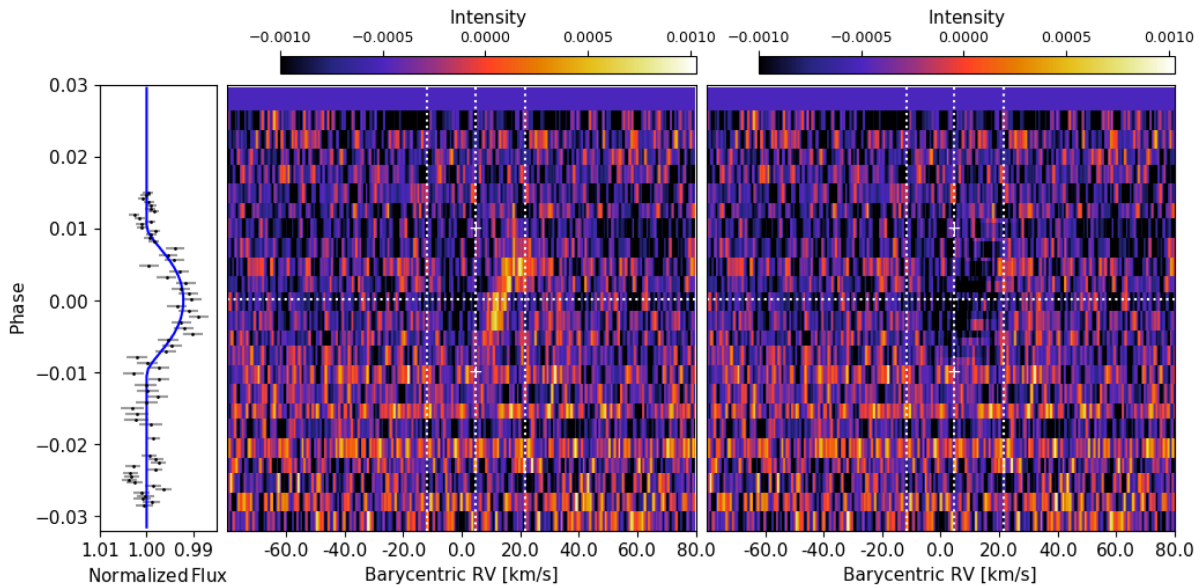


Figure 4. Middle: The line profiles through transit, with the average of the out-of-transit CCFs subtracted. We interpret this tomogram as showing a prograde-moving planet signal in the red-shifted section of the tomogram. Right: The line profile residuals after subtracting the planet model. In both of these panels, the white dotted vertical lines mark the positions of the γ velocity of the system and the positions of $\gamma \pm v \sin i_*$. The phase of mid-transit is marked by the white horizontal dotted line. The white + symbols indicate the beginning and end of the transit event, calculated using the ephemeris obtained in the adopted solution. Left: The TRAPPIST-South lightcurve taken simultaneously with the tomographic observation.

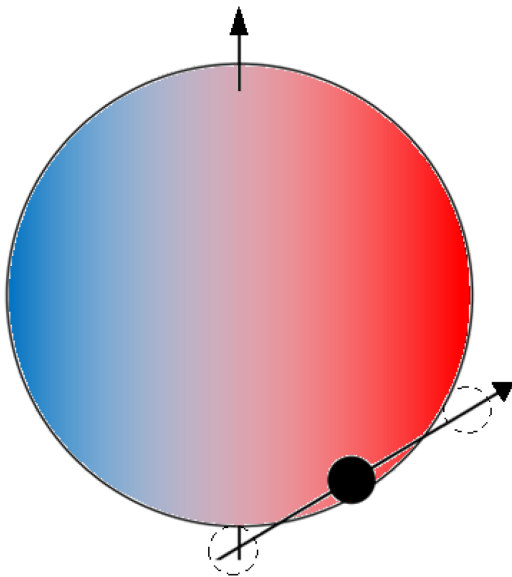


Figure 5. The transit chord calculated from the fitted values of R_p , R_* , b , and λ (see Table 3). The dashed circles show the positions of the planet at first and fourth contacts.

better than loosely constraining the radius to $R_p = 1.3 \pm 0.5 R_{\text{Jup}}$, which is consistent with that of an inflated hot Jupiter.

The mass of WASP-174b is also uncertain, since the hot host star limits the accuracy and precision of radial-velocity measurements. We report only an upper limit of $1.3 M_{\text{Jup}}$, so again WASP-174b is most likely a fairly typical inflated hot Jupiter. It may be possible, however, to constrain the mass further with some more precise RV measurements taken out-of-transit using HARPS.

At $V=11.9$, WASP-174 is the faintest hot-Jupiter system for which the shadow of the planet has been detected by tomographic

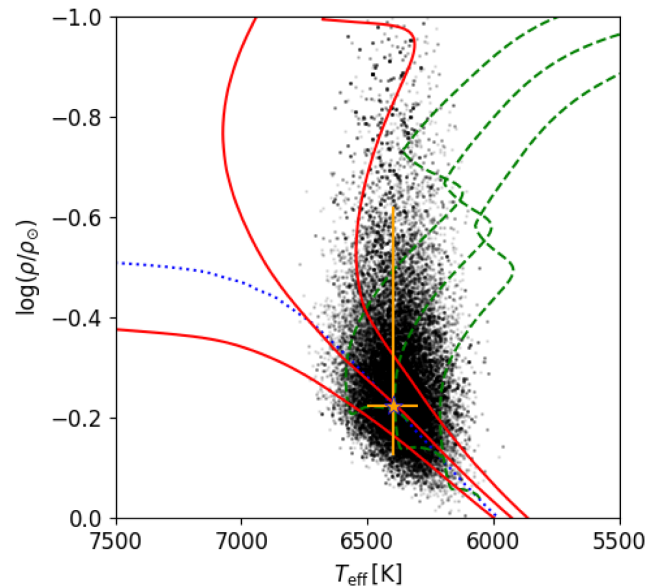


Figure 6. The best-fitting evolutionary tracks and isochrones of WASP-174 obtained using BAGEMASS. Black points: Individual steps in the MCMC. Dotted blue line: Zero-Age Main Sequence (ZAMS) at best-fitting $[\text{Fe}/\text{H}]$. Green dashed lines: Evolutionary track for the best-fitting $[\text{Fe}/\text{H}]$ and mass, plus 1σ bounds. Red lines: Isochrone for the best-fitting $[\text{Fe}/\text{H}]$ and age, plus 1σ bounds. Orange star: Measured values of T_{eff} and ρ_* for WASP-174 obtained in the spectral and photometric analyses, respectively.

methods. The next faintest are Kepler-448 at $V=11.4$ (Bourrier et al. 2015) and HAT-P-56 at $V=10.9$ (Huang et al. 2015; Zhou et al. 2016b), which was initially confirmed with radial velocity measurements.

HAT-P-56b is also comparable in that it has a near-grazing transit with an impact parameter of $b = 0.873_{-0.006}^{+0.004}$ (Huang et al. 2015),

which compares with $b = 0.94 \pm 0.03$ for WASP-174b. As with our work, the tomographic planet trace for HAT-P-56b is faint and possibly shows evidence for getting fainter when the planet is only partially occulting the star (i.e. at the beginning and end of the transit, Zhou et al. 2016b).

ACKNOWLEDGEMENTS

WASP-South is hosted by the South African Astronomical Observatory and we are grateful for their ongoing support and assistance. Funding for the Wide Angle Search for Planets (WASP) comes from consortium universities and from the UK's Science and Technology Facilities Council (STFC). The Euler Swiss telescope is supported by the Swiss National Science Foundation (SNF). TRAPPIST-South is funded by the Belgian Fund for Scientific Research (Fond National de la Recherche Scientifique, FNRS) under the grant FRFC 2.5.594.09.F, with the participation of the SNF. We acknowledge use of the European Southern Observatory 3.6-m/HARPS under program 096.C-0762. MG is FNRS Research Associate, and EJ is FNRS Senior Research Associate. The research leading to these results has received funding from the European Research Council under the FP/2007-2013 ERC grant agreement no. 336480, and from the ARC grant for Concerted Research Actions, financed by the Wallonia–Brussels Federation. This work was also partially supported by a grant from the Simons Foundation (ID 327127 to Didier Queloz).

REFERENCES

- Arcangeli J. et al., 2018, *ApJ*, 855, L30
 Baranne A. et al., 1996, *A&AS*, 119, 373
 Beatty T. G., Madhusudhan N., Tsiaras A., Zhao M., Gilliland R. L., Knutson H. A., Shporer A., Wright J. T., 2017, *AJ*, 154, 158
 Blackwell D. E., Shallis M. J., 1977, *MNRAS*, 180, 177
 Bourrier V. et al., 2015, *A&A*, 579, A55
 Brown D. J. A. et al., 2017, *MNRAS*, 464, 810
 Burdanov A., Delrez L., Gillon M., Jehin E., Speculoos T., Trappist Teams, 2017, SPECULOOS Exoplanet Search and Its Prototype on TRAPPIST. Springer International Publishing, Cham, p. 1
 Claret A., 2000, *A&A*, 363, 1081
 Claret A., 2004, *A&A*, 428, 1001
 Collier Cameron A. et al., 2006, *MNRAS*, 373, 799
 Collier Cameron A. et al., 2007, *MNRAS*, 380, 1230
 Collier Cameron A., Bruce V. A., Miller G. R. M., TriAUD A. H. M. J., Queloz D., 2010a, *MNRAS*, 403, 151
 Collier Cameron A. et al., 2010b, *MNRAS*, 407, 507
 Crouzet N. et al., 2017, *AJ*, 153, 94
 Dai F., Winn J. N., 2017, *AJ*, 153, 205
 Doyle A. P. et al., 2013, *MNRAS*, 428, 3164
 Doyle A. P., Davies G. R., Smalley B., Chaplin W. J., Elsworth Y., 2014, *MNRAS*, 444, 3592
 Enoch B., Collier Cameron A., Parley N. R., Hebb L., 2010, *A&A*, 516, A33
 Evans T. M. et al., 2017, *Nature*, 548, 58
 Fortney J. J., Lodders K., Marley M. S., Freedman R. S., 2008, *ApJ*, 678, 1419
 Gaia Collaboration et al., 2016, *A&A*, 595, A1
 Gaia Collaboration et al., 2018, *A&A*, 616, A1
 Gaudi B. S. et al., 2017, *Nature*, 546, 514
 Gibson N. P., Nikolov N., Sing D. K., Barstow J. K., Evans T. M., Kataria T., Wilson P. A., 2017, *MNRAS*, 467, 4591
 Gillon M. et al., 2010, *A&A*, 511, A3
 Gillon M. et al., 2012, *A&A*, 542, A4
 Gray R. O., Corbally C. J., 2014, *AJ*, 147, 80
 Hartman J. D. et al., 2015, *AJ*, 150, 197
 Hartman J. D. et al., 2016, *AJ*, 152, 182
 Hellier C. et al., 2011, EPJ Web Conf., 11, 01004
 Heng K., Showman A. P., 2015, *Annu. Rev. Earth Planet. Sci.*, 43, 509
 Hirano T., Suto Y., Winn J. N., Taruya A., Narita N., Albrecht S., Sato B., 2011, *ApJ*, 742, 69
 Huang C. X. et al., 2015, *AJ*, 150, 85
 Jehin E. et al., 2011, *The Messenger*, 145, 2
 Johnson M. C. et al., 2018, *AJ*, 155, 100
 Kraft R. P., 1967, *ApJ*, 150, 551
 Kreidberg L. et al., 2015, *ApJ*, 814, 66
 Kreidberg L. et al., 2018a, *AJ*, 156, 17
 Kreidberg L., Line M. R., Thorngren D., Morley C. V., Stevenson K. B., 2018b, *ApJ*, 858, L6
 Lund M. B. et al., 2017, *AJ*, 154, 194
 Maxted P. F. L. et al., 2011, *PASP*, 123, 547
 Maxted P. F. L., Serenelli A. M., Southworth J., 2015, *A&A*, 575, A36
 Mazeh T., Perets H. B., McQuillan A., Goldstein E. S., 2015, *ApJ*, 801, 3
 Munari U., Zwitter T., 1997, *A&A*, 318, 269
 Parmentier V. et al., 2018, *A&A*, preprint (arXiv:1805.00096)
 Pepe F. et al., 2002, *The Messenger*, 110, 9
 Pollacco D. et al., 2008, *MNRAS*, 385, 1576
 Pont F., Husnoo N., Mazeh T., Fabrycky D., 2011, *MNRAS*, 414, 1278
 Queloz D. et al., 2001, *The Messenger*, 105, 1
 Sestito P., Randich S., 2005, *A&A*, 442, 615
 Siverd R. J. et al., 2018, *AJ*, 155, 35
 Smalley B. et al., 2011, *A&A*, 526, A130
 Stassun K. G., Torres G., 2018, *ApJ*, 862, 61
 Stevenson K. B., Bean J. L., Madhusudhan N., Harrington J., 2014, *ApJ*, 791, 36
 Talens G. J. J. et al., 2017, *A&A*, 606, A73
 Talens G. J. J. et al., 2018, *A&A*, 612, A57
 Temple L. Y. et al., 2017, *MNRAS*, 471, 2743
 Torres G., Andersen J., Giménez A., 2010, *A&A Rev.*, 18, 67
 TriAUD A. H. M. J., 2017, *The Rossiter-McLaughlin Effect in Exoplanet Research*. Springer International Publishing, Cham, p. 1
 Valsecchi F., Rasio F. A., 2014, *ApJ*, 786, 102
 Weiss A., Schlattl H., 2008, *Ap&SS*, 316, 99
 Winn J. N., Fabrycky D., Albrecht S., Johnson J. A., 2010, *ApJ*, 718, L145
 Wyttenbach A., Ehrenreich D., Lovis C., Udry S., Pepe F., 2015, *A&A*, 577, A62
 Yan F., Henning T., 2018, *Nature Astron.*, preprint (arXiv:1807.00869)
 Zhou G. et al., 2016a, *AJ*, 152, 136
 Zhou G., Latham D. W., Bieryla A., Beatty T. G., Buchhave L. A., Esquerdo G. A., Berlind P., Calkins M. L., 2016b, *MNRAS*, 460, 3376
 Zhou G. et al., 2017, *AJ*, 153, 211

This paper has been typeset from a $\text{\TeX}/\text{\LaTeX}$ file prepared by the author.